Characterization of a 5 kW Solid Oxide Fuel Cell Stack Using Power Electronic Excitation

John J. Cooley *Student Member, IEEE*, Eric Seger, Steven Leeb *Fellow, IEEE*,
and Steven R. Shaw *Senior Member, IEEE*

***Abstract*—Fuel cells have attracted great interest as a means of clean, efficient conversion of chemical to electrical energy. This paper demonstrates the identification of both non-parametric and lumped circuit models of our stack in response to a test signal introduced by control of a power electronic circuit. This technique could be implemented on-line for continuous condition assessment of the stack, as it delivers power. The results show typical data from the stack, comparison of model and measured data, and whole-stack impedance spectroscopy results using a power electronic system to provide excitation. Run-time excitation currents for the spectroscopy measurement are generated by a hybrid power system controlling the flow of power from the fuel cell and a secondary power source to a fixed resistive load. The hybrid power system generates small-signal currents at the fuel cell terminals while the load current itself is largely unaffected by the impedance spectroscopy measurement.**

***Index Terms*—Fuel Cells, Impedance Spectroscopy, Prognostics, Power Electronics**

I. Introduction

There is an increasing realization that the commercial viability of fuel cells depends on work to enhance reliability and durability [1], [2]. Much of the effort to enhance fuel cell robustness is appropriately focused on materials development using traditional materials science methodologies, e.g. single cell or even single component testing in controlled environments thought to be similar to the conditions inside a stack. However, there is also interest in understanding degradation phenomena that can occur as fuel cells are integrated into real systems. As an example, in [3], Ramschak et al provide a method to detect the failure of a single cell within a stack by analyzing the harmonic distortion on the stack voltage. Similarly, in [4] Gemmen et al study the impact of inverter load dynamics on a fuel cell, with the conclusion that stack / inverter interaction is significant in the operating conditions and long term behavior of the stack.

In our SOFC stack, and in many similar fuel cell applications, it is neither feasible nor desirable to remove the stack from service for the purpose of connecting impedance spectroscopy instrumentation. However, in principle, it is not necessary to remove the load provided that a sufficiently rich test signal can be introduced in addition to the load, as in [5]. This paper demonstrates the use of power electronics to impose a test signal while delivering power to a load. This characterization consists of calculations of whole stack impedance spectroscopy and time-domain model parameters, using both the switching waveform, or "ripple", of the power electronics connected to the stack and an exogenous excitation. This method requires only instrumentation at the stack electrical terminals, and could be integrated with the controls of existing power electronics to provide non-invasive, low cost stack prognostics. The underlying motivation of this work, not directly addressed in this paper, is that we may ultimately be able to improve reliability and mitigate materials challenges through controls at the electrical terminals that are richly informed of the state of the stack.

The paper begins with an overview of electrochemical impedance spectroscopy (EIS) and associated system identification considerations in section II-B. In section II-C we suggest a lumped parameter, time-domain model and identification procedure for the small signal response of the stack. In section III, we discuss the design considerations and circuit modeling of the hybrid power system used to generate the signals for impedance spectroscopy. The experimental setup is described in section IV, and results are provided in section V.

II. Fuelcell Operation and Modeling

A. Fuel Cell Overview

Figure 1 is a conceptual illustration of the energy conversion mechanism in a solid oxide fuel cell. The cell comprises three layers. The cathode (right) is a porous, electrically conductive material. Molecular oxygen is reduced to oxygen ions in the cathode, with electrons supplied by the external circuit. These oxygen ions move readily from the cathode through a dense electrolyte, which is ion-conducting but is an electronic insulator. At appropriate temperatures, typically in the vicinity of 750 C, the electrolyte becomes conductive to oxygen by means of oxygen vacancies in the lattice structure of the material. The anode layer is another porous, electrically conductive cermet material. Oxygen ions arriving from the electrolyte serve to oxidize fuel and release their electrons to the external circuit. Typical materials for the cathode/electrolyte/anode structure include lanthanum strontium maganate (LSM), ytria stabilized zirconia (YSZ), and nickel/YSZ cermet, respectively. While the overall reaction in Fig. 1 shows hydrogen as a fuel and water as a product, a basic advantage of SOFC technology is that the electrolyte is an oxygen ion conductor. This allows the use of fuels containing carbon, as opposed hydrogen-conducting fuel cell technologies.

Fig. 2 shows a photograph of the actual stack used for testing in this paper. The stack is a 5kW nominal, Fuel Cell Technologies / Siemens Alpha-8 tubular solid oxide fuel cell using city natural gas as a fuel. The vents at the top are for intake and exhaust, and this particular unit was also configured with a recuperator that could be used to heat water for a combined heat and power application. This unit is designed for three-phase grid-tie operation. However, for purposes of this study we were able to access and connect power electronics to the terminals of

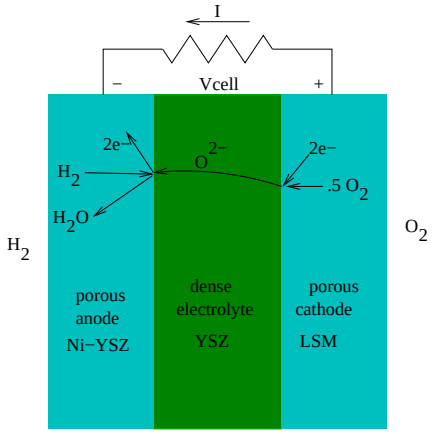

Fig. 1: Conceptual diagram of SOFC energy conversion.

the stack and monitor the response of the stack to test signals imposed by those power electronics.

Fig. 2: A 5 kW Siemens / Fuel Cell Technology stack used for testing.

B. Fuel Cell Impedance Spectroscopy

Electrochemical impedance spectroscopy models the AC electrical terminal response of a fuel cell (or other electrochemical system) in the vicinity of an operating point as a linear impedance $Z(j\omega)$. In particular, for cell voltage and current

$$v_c(t) = V_o + v(t) \quad (1)$$

$$i_c(t) = I_0 + i(t), \quad (2)$$

at a DC operating point V_0, I_0, the impedance captures the frequency domain relationship between the small signal quantities $v(t)$, $i(t)$. Use of this model presumes that the cell responds linearly over the range of excitation in the vicinity of the bias point, i.e. that excitation at a single frequency produces a response at that frequency.

Impedance spectroscopy results are generally presented using a Nyquist plot showing real and complex parts of the impedance with frequency as an implicit argument. An electrochemist can recognize the shapes characteristic of processes in the Nyquist diagram [6]. Practitioners often extend this non-parametric analysis by fitting lumped-parameter circuit models, in the frequency domain, and in some cases associate physical processes with individual circuit elements. In [7], a parameterized impedance spectroscopy model is used to synthesize an equivalent circuit of an SOFC. Other examples include the analysis of a PEM cell in [8] and the application to an SOFC cell in [7]. Frequencies of 0.01Hz to 1MHz are generally used for studying SOFC systems [2]. For a survey of impedance spectroscopy in fuel cells, see [9].

Under sufficiently rich excitation, an estimate $\hat{Z}(j\omega)$ of the impedance response can be extracted from the terminal voltage and current of a cell. In particular, an impedance estimate is

$$\hat{Z}(j\omega) = \frac{\hat{V}_c(j\omega)}{\hat{I}_c(j\omega)}, \quad |\omega| > 0, \quad (3)$$

where $\hat{V}_c(j\omega)$ and $\hat{I}_c(j\omega)$ are estimates of the spectral content of the electrical terminal responses $v_c(t)$ and $i_c(t)$. The process of estimating spectral content of signals using sampled data and discrete-time Fourier transform techniques, including windowing and other considerations, is reviewed in [10] among others. The excitation $i_c(t)$ imposed at the electrical terminals must be broadly exciting, in the sense of having significant power at frequencies where it is desired to have a good estimate of $Z(j\omega)$. If $\hat{I}_c(j\omega)$ at some frequency is small or dominated by noise, the variance in $\hat{Z}(j\omega)$ can be large. In practice, we avoid this by not evaluating $Z(j\omega)$ for frequencies where the signal content in the $I_c(j\omega)$ is small in comparison to a threshold.

C. Parametric Modeling and Identification

In addition to impedance spectroscopy, it is sometimes useful to model fuel cell responses using a parameterized model, often in the form of a differential equation that represents specific physical processes. For example, Hall [11] develops a transient model of a tubular SOFC including electrochemical, thermal, and mass flow elements. Wang et al. [12] develop a dynamic model for a proton exchange membrane fuel cell using electrical circuit elements, and Pasricha et al. [13] provide a dynamic electrical terminal model of a proton exchange membrane fuel cell. A challenge in developing parametric, physically-baed models of fuel cells is to restrict the phenomena in the model to those which are well supported by the observations.

With preliminary, non-parametric observations in mind, we propose a very simple three-parameter model of the stack, i.e.

$$v(t) = V_{oc} - Ri(t) - Ls\, i(t), \quad (4)$$

where $v(t)$ is the stack voltage, $i(t)$ is the stack current, V_{oc} is the open circuit stack voltage, R is a resistance, L is a inductance, and s is the $\frac{d}{dt}$ operator.

The parameters of (4) are conveniantly estimated using the operator substitution technique in [10]. The low-pass filter operator

$$\lambda = \frac{1}{1 + s\tau}. \quad (5)$$

can be manipulated to isolate s, i.e.

$$s = \frac{1-\lambda}{\lambda\tau}. \tag{6}$$

Substituting s into (4) and rearranging so λ appears in the numerator provides

$$\lambda\tau V_{oc} - \tau\lambda i(t)R + (\lambda-1)i(t)L = \tau\lambda v(t). \tag{7}$$

This is appealing because $\lambda\tau$, $\lambda i(t)$, and $\lambda v(t)$ can be evaluated using a discrete-time implementation of λ applied to the data. These quantities can be arranged in a least-squares tableau to obtain estimates for the parameters V_{oc}, R, and L. Setting $\lambda\tau V_{oc}$ to the final value, we form the following equations

$$\begin{pmatrix} \tau & -\tau\lambda i[1] & (\lambda-1)i[1] \\ \tau & -\tau\lambda i[2] & (\lambda-1)i[2] \\ \vdots & \vdots & \vdots \\ \tau & -\tau\lambda i[n] & (\lambda-1)i[n] \end{pmatrix} \begin{pmatrix} V_{oc} \\ R \\ L \end{pmatrix} = \begin{pmatrix} \tau\lambda v[1] \\ \tau\lambda v[2] \\ \vdots \\ \tau\lambda v[n] \end{pmatrix} \tag{8}$$

to estimate the parameters of (4).

III. Power Electronics

We can demonstrate the concept of run-time electrochemical impedance spectroscopy (EIS) in a hybrid power system with off-the-shelf power converters. A simplified connection diagram for our EIS-capable hybrid power system is shown in Figure 3a. In our system, the control signal drives the trim pin of the Buck converter module in the fuel cell leg (the upper leg in Figure 3a).

A. Small-signal Behavior

Conceptually, the hybrid system enables run-time fuel cell diagnostics by providing a means for exciting the fuel cell with a small-signal current originating at the secondary source (the battery in this case), while the load current itself is largely unaffected by the EIS measurement. The small-signal current paths corresponding to this behavior are depicted in Figure 3b.

We can analyze the small-signal behavior of such a system starting from Middlebrook's linearized canonical models of CCM-operated power converters [14]. A parallel development could be carried out if the converters operate in DCM by using the corresponding models for DCM-operated converters [15].

1) ***Middlebrook's Linearized Models of Power Converters:*** In reference [14], Middlebrook develops linearized circuit models that can be used to represent the input, output and control properties of any switching power converter.

To that end, Middlebrook demonstrates how CCM-operated converters can be manipulated into one fixed topology and DCM-operated converters into another fixed topology in references [14], [15], [18]. For example, the basic elements of a typical power converter are shown in Figure 4a. In Figure 4b, the buck converter has been replaced with the linearized canonical circuit model developed by Middlebrook in [14]. [1]

The canonical circuit model consists of three pieces (in boxes): an ideal transformer that represents the converter's ideal voltage and current transformation[2], an effective low-pass filter

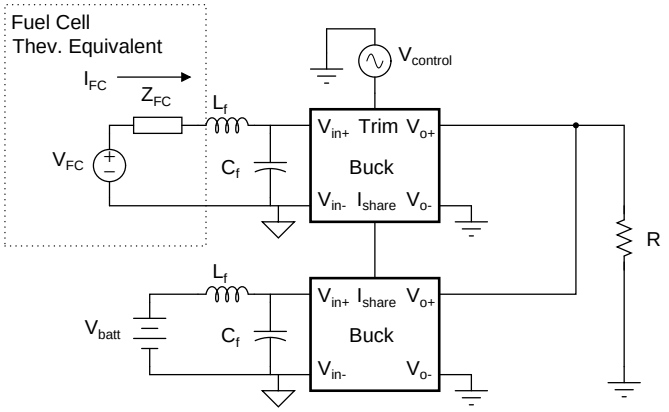

(a) A simplified connection diagram of the hybrid system built from off-the-shelf components.

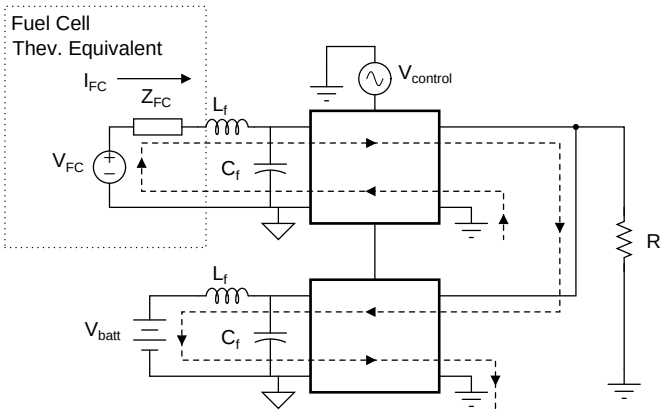

(b) Small-signal current paths for EIS excitation signals.

Fig. 3: A hybrid power system with EIS functionality built from off-the-shelf components.

at the output that includes the effects of the energy storage elements involved in the switching action of the converter, and dependent current and voltage sources that capture the effect of the control signal, $\hat{d}$. Reducing a converter to this "fixed topology" means that a linearized input-output and control description of any converter reduces to looking up the, perhaps frequency-dependent values for each of the model parameters as in Table I [14], [17]. In [19], the author shows how the values in Table I for a *generalized load* can be taken from similar canonical model parameters that were previously calculated for a converter driving a *fixed load* R.

TABLE I: Canonical Model Parameters for the Buck, Boost and Buck-Boost with a general load [17], [19]

Converter	$M(D)$	L_e	$e(s)$	$j(s)$
Buck	D	L	$\frac{V}{D^2}$	I
Boost	$\frac{1}{D'}$	$\frac{L}{D'^2}$	$V\left(1-\frac{sLI}{D'^2V}\right)$	$\frac{I}{D'^2}$
Buck-Boost	$-\frac{D}{D'}$	$\frac{L}{D'^2}$	$-\frac{V}{D^2}\left(1-\frac{sDLI}{D'^2V}\right)$	$-\frac{I}{D'^2}$

[1] According typical conventions, the hats (ˆ) denote small-signal quantities.

[2] the straight line and the wavy line drawn on the transformer element in Figure 4b are intended to indicate DC and AC respectively.

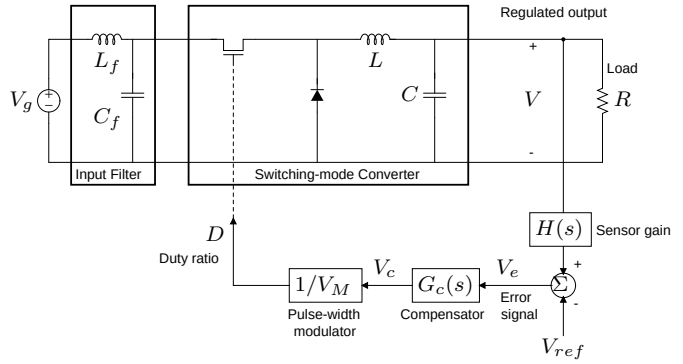

(a) Basic Elements of a switching-mode regulator. The LC input filter and buck converter are shown as typical realizations [16].

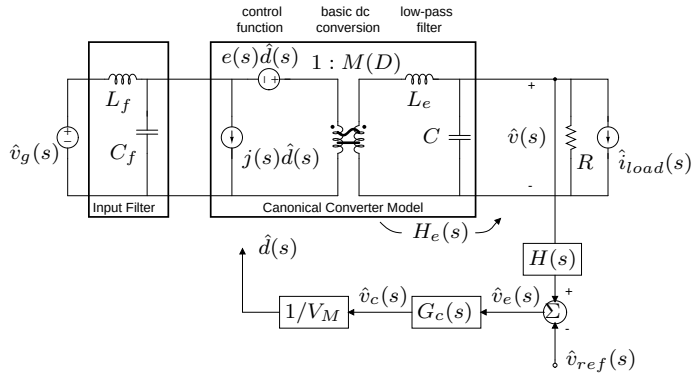

(b) A small-signal regulator model using Middlebrook's linearized canonical circuit model of the power converter [16]. Hats (ˆ) denote small-signal quantities.

Fig. 4: Canonical circuit modeling developed in references [14], [16] and [17].

*2) **A Linearized Model of the Hybrid Power System:*** Having configured the system in Figure 3 so that its small-signal behavior is similar to that of two parallel converters under voltage-mode feedback control, we can build the corresponding linearized model of the hybrid power system shown in Figure 5.

In reference [19], the author uses a linear superposition and replacement of dependent sources approach to derive the closed-loop transfer functions describing the small-signal behavior of a hybrid power system like that in Figure 5. For instance, taking the input $\hat{v}_{ref1}$ as the control signal, assuming two identical converters, and neglecting the effects of the input filters on the system dynamics, the author shows that the transfer functions of interest here are:

$$\frac{\hat{v}}{\hat{v}_{ref1}} = \frac{1}{H}\frac{\lambda T}{1+2T\lambda} \tag{9}$$

$$\frac{\hat{i}_{o2}}{\hat{i}_{o1}} = -\frac{\lambda T}{HZ_e}\left(\frac{T(2\lambda-1)}{1+2T\lambda}-1\right) \tag{10}$$

$$\frac{\hat{i}_{in1}}{\hat{v}_{ref1}} = j(s)F_m G_c(s)\left(1-H\frac{\hat{v}}{\hat{v}_{ref1}}\right)+M(D)\frac{\hat{i}_{o1}}{\hat{v}_{ref1}} \tag{11}$$

$$\frac{\hat{i}_{o1}}{\hat{v}_{ref1}} = \frac{T}{HZ_e}\left(\frac{\lambda T(2\lambda-1)}{1+2T\lambda+1-\lambda}\right), \tag{12}$$

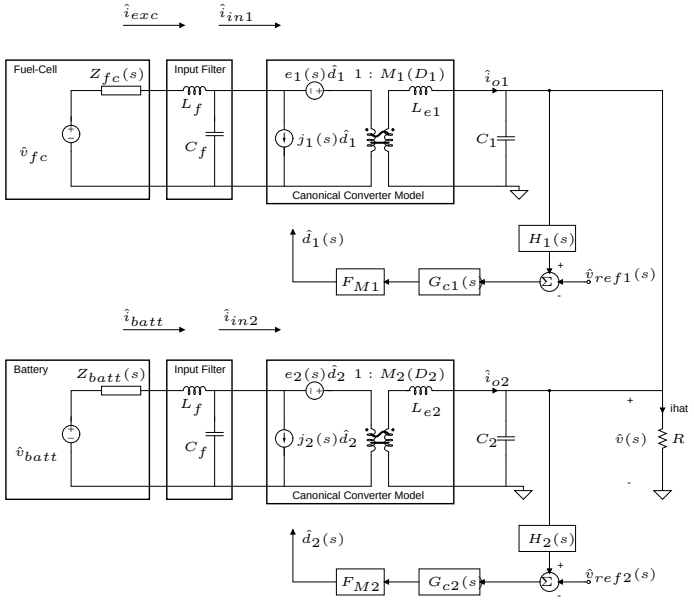

Fig. 5: A small-signal hybrid system modeled using the canonical circuit model of CCM-operated power converters.

where

$$Z_e = sL_e \tag{13}$$

$$\lambda' = Z_e + Z_e||R \tag{14}$$

$$\lambda = \frac{Z_e||R}{\lambda'} \tag{15}$$

and the loop transfer function is defined as

$$T = HG_cF_Me(s)M(D). \tag{16}$$

Such a model can be validated by comparing the calculated expressions in (9)-(11) to simulations of the system in Figure 5 (LTSPICE) as in Figures 7, 8, and 9. The magnitude and phase plots of $\hat{i}_{o2}/\hat{i}_{o1}$ in Figure 7, confirm our intuition that, at low frequency, the currents out of the two converters are equal and opposite (small-signal currents flow out of one and into the other). This behavior corresponds to the time-domain data shown in the scope shot of Figure 6, taken from the experimental system of Figure 3.

Figures 8 and 9 show that the transconductance from the control voltage, $\hat{v}_{ref1}$, to input current, $\hat{i}_{in1}$, is large and the corresponding load voltage perturbation, $\hat{v}$, is small. This amounts to the desired characteristic of an EIS-capable hybrid power system that the load voltage will be largely unaffected by the run-time EIS behavior.

B. Input Filters and System Stability

The design of the input filters in Figure 5 presents some interesting power electronics design challenges. The classic results concerning the effect of a "post-facto" input filter on converter performance are derived by Middlebrook from an application of the extra element theorem in [16], [17], [20]. The resulting design constraints are typically quoted as a set of impedance inequalities that, if met, ensure negligible degradation of converter performance. However, in our hybrid power system, designed to enable EIS of the fuel cell, we have a

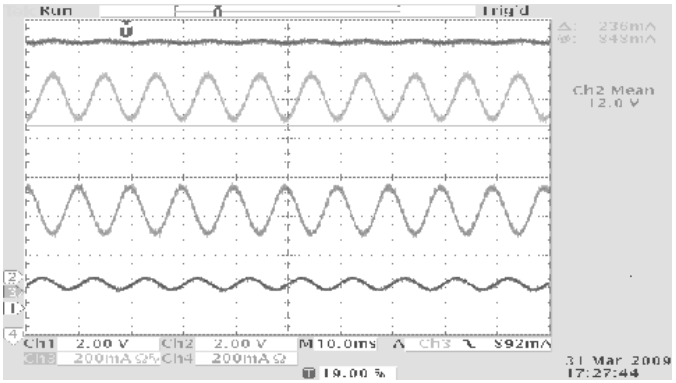

Fig. 6: An oscilloscope screen shot showing the battery and fuel cell currents during run-time EIS (≈100 Hz). Top to bottom: load voltage (ch2), fuel cell current (ch3), battery current (ch4), control signal (ch1). The excitation current flows out of the battery terminals and into the fuel cell terminals while the load voltage is largely unaffected by the run-time EIS measurement.

more complicated set of design constraints that must be met. Specifically, the input filters must not only be designed for system stability but must also pass excitation currents from the converter inputs to the fuel cell terminals. Meanwhile, the analytical results presented by Middlebrook in [16], [20], must be extended so that they may be applied to the hybrid power system (paralleled converter) case.

1) ***Middlebrook's Application of the EET for Input Filter Design:*** The treatment of an input filter as a "post-facto" element in a power converter design is a likely outcome of natural design processes. However, this treatment is also *analytically* advantageous. The converter can be designed without the input filter and then the Extra Element Theorem applied to determine the perturbation on the converter dynamics without ever analyzing the full system. The extra element theorem, best summarized by Middlebrook in [21], allows us to replace one cumbersome and uninsightful calculation, with a few simple and elegant calculations.

The extra element theorem follows from an application of the principle of "null double injection" to a linear circuit [21]. Upon addition of an extra element to the circuit, the transfer function of interest, completely defined by an input and output variable in the circuit, can be modified by calculating the impedance seen at the "extra element port" under *two* special cases. The first special case corresponds to null-double injection and is the impedance seen at the extra element port when the transfer function input variable is directed in such a way that the transfer function output variable is nulled (equal to zero). The result is the "null-condition" impedance, $Z_{n-c}(s)$. The second special case corresponds to the open-loop behavior and is the impedance at the extra element port when the transfer function input signal is deactivated (set to zero), leading to $Z_{o-l}(s)$. Fundamentally, the extra element theorem uses the unique information obtained about the circuit by calculating those two special-case impedances to derive the circuit's interaction with the extra element itself. The primary result of the ensuing mathematical manipulations is a statement of the correction

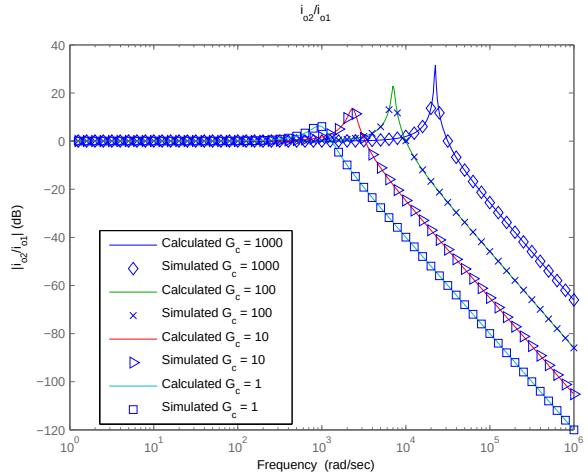

(a) Magnitude

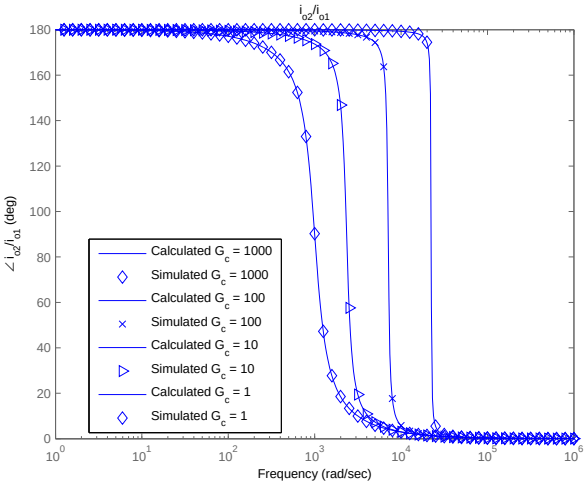

(b) Phase

Fig. 7: i_{o2}/i_{o1}.

factor that multiplies the original transfer function. For a series extra element (one that replaces a short-circuit in the original circuit), the correction factor is

$$CF = \left(\frac{1 + \frac{Z_o(s)}{Z_{n-c}(s)}}{1 + \frac{Z_o(s)}{Z_{o-l}(s)}} \right), \tag{17}$$

in which $Z_{n-c}(s)$ is the special-case impedance calculated for the null condition, $Z_{o-l}(s)$ is the special-case impedance calculated for the open-loop condition and $Z_o(s)$ is the impedance of the extra element itself.

While the converter transfer function can be defined by any arbitrarily defined input variable and any corresponding output variable, some notable converter transfer functions are represented within the dashed box in Figure 10 adapted from [17]. The converter transfer function, $G_{vd}(s)$, is usually of particular interest because it is "in the loop," i.e. the dynamics of $G_{vd}(s)$ directly impact the stability of the regulator. Upon addition of an input filter, $G_{vd}(s)$ is modified by the correction factor in (17), in which $Z_{n-c}(s)$ and $Z_{o-l}(s)$ can be calculated

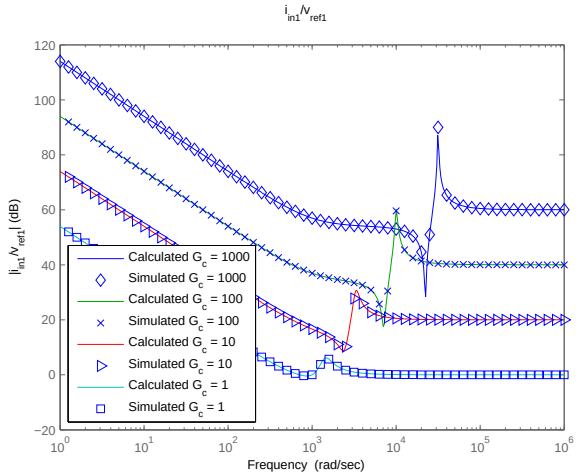

Fig. 8: $|i_{in1}/v_{ref1}|$.

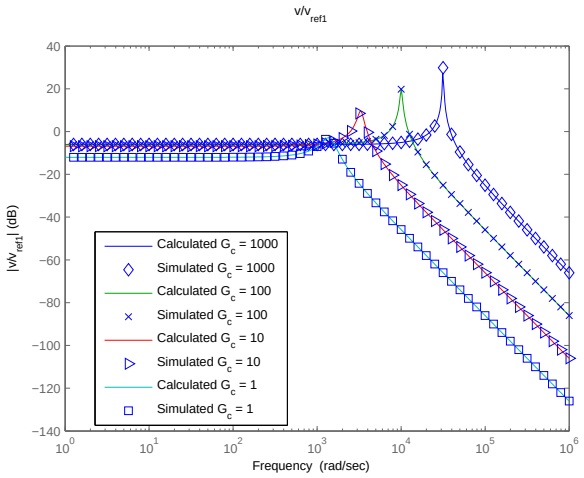

Fig. 9: $|v/i_{ref1}|$.

from the circuit in Figure 11.

The null-condition does not generally allow us to simplify the circuit topologically, or even to easily write down a closed-form expression of the control signal that leads to the nulled output signal.[3] But, the null-condition often allows us to make observations about the circuit that simplify the calculation, not of the control signal itself, but of the impedance at the extra element port as a result of the conditions that the control signal must impose on that circuit to null the output.

For example, to calculate $Z_{n-c}(s)$ for correcting $G_{vd}(s)$, the transfer function from $\hat{d}$ to $\hat{v}$, in the circuit of Figure 11, we deactivate the other independent inputs, $\hat{v}_g$ and $\hat{i}_{load}$, and null the output $\hat{v} \rightarrow 0$. The analysis is simplified by realizing that for a nulled output, the small-signal voltage across the load impedance is zero so no small-signal current flows through the load. Therefore, no current flows through L_e or through the secondary winding of the ideal transformer. The primary winding current is therefore also zero. Because the current

[3]Note that it would (generally) be a misinterpretation of the null-condition to simply short-circuit the output of the converter in Figure 11 and, in most cases, would lead to different and incorrect results.

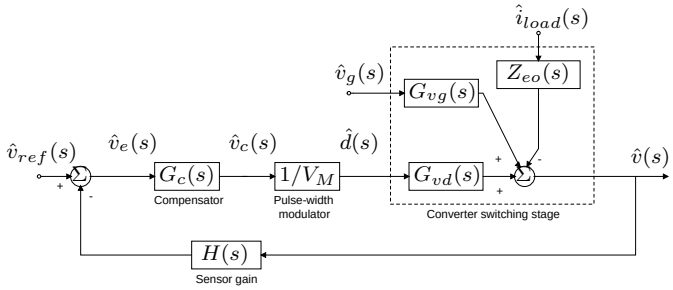

Fig. 10: A dynamical block diagram of a voltage-mode feedback regulated converter. [17]

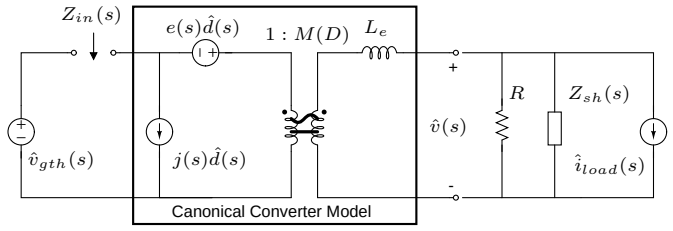

Fig. 11: The linearized converter model with three independent inputs, $\hat{v}_g$, $\hat{d}$, and $\hat{i}_{load}$. for calculating the special-case impedances in the extra element correction factors.

through L_e is zero, the voltage across it is also zero and the zero-valued (nulled) output voltage appears at the secondary winding of the ideal transformer. Therefore, the input voltage and current are simply $-e(s)\hat{d}(s)$ and $j(s)\hat{d}(s)$, respectively and the input impedance in this case is $Z_{n-c}(s) = -e(s)/j(s)$.

In [19], the author shows that the three converter transfer functions represented in the dashed box of Figure 10, can be corrected using the generalized results in Table II. Those results hold for CCM-operated converters, and the special-case impedances can be found by looking up the canonical model parameters in a table such as Table I.

TABLE II: Generalized Input Filter Design Constraints adapted from [19]

Special-case	Impedance	Generalized Value	Transfer Function
open-loop	$Z_D(s)$	$\frac{sL_e+R\|\|Z_{sh}(s)}{M(D)^2}$	All
null-condition	$Z_N(s)$	$\frac{-e(s)}{j(s)}$	$G_{vd}(s)$
	$Z_e(s)$	$\frac{sL_e}{M(D)^2}$	$Z_{eo}(s)$
	$Z_g(s)$	∞	$G_{vg}(s)$

The correction factor can be used to directly evaluate the degradation of converter transfer functions. However, it is immediately obvious from the expression of the correction factor in (17), that if the following inequalities are met, the input filter will have a negligible impact on the converter dynamics [16], [20]:

$$|Z_o| << |Z_{n-c}| \quad (18)$$

$$|Z_o| << |Z_{o-l}|. \quad (19)$$

Meeting the first inequality will ensure that the filter output impedance is always less than the negative incremental resistance presented by the inputs of a regulated converter. For instance, from Tables I and II, $Z_{n-c}(s)$ for the Buck converter is $-V/ID^2$. The same result can be derived for a lossless ($P_{out} = P_{in}$), perfectly-regulated converter ($V_{out} = V =$ const.) with a fixed load ($I_{out} = I =$ const.) as follows:

$$Z_{n-c}(s) = \frac{\partial V_{in}}{\partial I_{in}} = \frac{\partial}{\partial I_{in}}\left(\frac{P_{out}}{I_{in}}\right) = -\frac{P_{out}}{I_{in}^2} = -\frac{V}{ID^2}. \quad (20)$$

A typical plot of the three impedances of interest in Figure 12 illustrates the design choices required to meet the inequalities in (18)-(19). In practice, meeting the inequality in (18) is often achieved for LC filter designs by using a damping leg (a series RC) shunting the input terminals to decrease the magnitude peaking in the LC filter output impedance. Meeting the second inequality (19) is usually achieved by setting the frequency of the 2nd-order peak in the input filter output impedance below that of the 2nd-order dip in the output filter input impedance (represented by $Z_{o-l}(s)$).

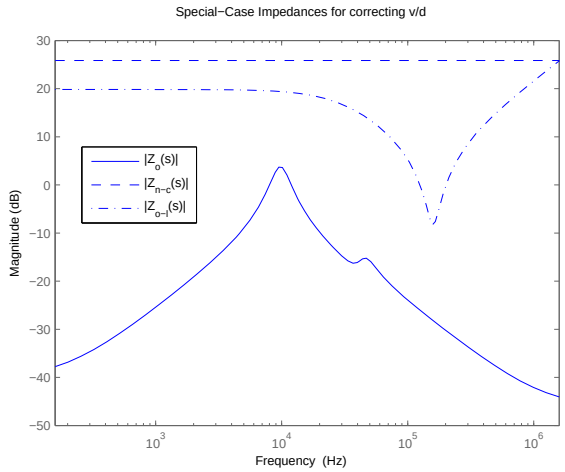

Fig. 12: A typical frequency plot of the special case impedances, $Z_{n-c}(s)$, $Z_{o-l}(s)$, and the input filter output impedance, $Z_o(s)$, for a single converter system.

While the concepts above were reviewed and developed for a single-converter system, the same concepts will be extended, in Section III-B2, to the two-converter case corresponding to the hybrid power system in Figure 5.

2) ***The 2EET Applied to the Hybrid Power System:*** In the hybrid power system of Figure 5, each converter is furnished by an input filter. Ignoring, for now, the particular feedback loops in that system, we can consider the circuit as a whole rather than as two separate converters. That system, like the single-converter system in Section III-B1 can be characterized by its open-loop transfer functions from any independent input to any output variable. Of particular interest, are the converter transfer functions that will be "in the loop" upon addition of feedback control. In Figure 5, those are the transfer functions from each duty ratio, $\hat{d}_1$ and $\hat{d}_2$, to the output voltage, $\hat{v}$, because of the voltage-mode feedback control depicted there.

Now, we must consider the effect on the converter transfer functions upon the simultaneous addition of *two* input filters to the overall system. To that end, the author in [19] applies the two extra element theorem to the system in Figure 5. In [22], Middlebrook presents the two extra element theorem (2EET), the principle result of which is the correction factor:

$$CF^{(i)} = \frac{1 + \frac{Z_1}{Z_{N1}|^{(i)}_{Z_2=0}} + \frac{Z_2}{Z_{N2}|^{(i)}_{Z_1=0}} + K_N^{(i)}\frac{Z_1 Z_2}{Z_{N1}|^{(i)}_{Z_2=0} Z_{N2}|^{(i)}_{Z_1=0}}}{1 + \frac{Z_1}{Z_{D1}|^{(i)}_{Z_2=0}} + \frac{Z_2}{Z_{D2}|^{(i)}_{Z_1=0}} + K_D^{(i)}\frac{Z_1 Z_2}{Z_{D1}|^{(i)}_{Z_2=0} Z_{D2}|^{(i)}_{Z_1=0}}}, \quad (21)$$

where Z_1 and Z_2 are the output impedances of the first and second input filters respectively.[4] The interaction parameters can be written (they each have two possible forms) [22]:

$$K_N^{(i)} = \frac{Z_{N1}|^{(i)}_{Z_2=0}}{Z_{N1}|^{(i)}_{Z_2=\infty}} = \frac{Z_{N2}|^{(i)}_{Z_1=0}}{Z_{N2}|^{(i)}_{Z_1=\infty}} \quad (22)$$

$$K_D^{(i)} = \frac{Z_{D1}|^{(i)}_{Z_2=0}}{Z_{D1}|^{(i)}_{Z_2=\infty}} = \frac{Z_{D2}|^{(i)}_{Z_1=0}}{Z_{D2}|^{(i)}_{Z_1=\infty}}, \quad (23)$$

In [19], the author shows that analysis of the circuit in Figure 5 leads to the following special-case impedances for calculating the correction factor of the open-loop transfer function $\hat{v}/\hat{d}_1$:

$$Z_{N1}|^{(1)}_{Z_2=0} = \frac{-e_1(s)}{j_1(s)} \quad (24)$$

$$Z_{N2}|^{(1)}_{Z_1=0} = \frac{sL_{e2}}{M_2^2(D_2)} \quad (25)$$

$$Z_{D1}|^{(1)}_{Z_2=0} = \frac{sL_{e1} + \frac{sL_{e2}Z_L}{Z_L+sL_{e2}}}{M_1^2(D_1)} \quad (26)$$

$$Z_{D2}|^{(1)}_{Z_1=0} = \frac{sL_{e2} + \frac{sL_{e1}Z_L}{Z_L+sL_{e1}}}{M_2^2(D_2)}, \quad (27)$$

where Z_L is the total impedance shunting the converter outputs, i.e. $Z_L = R||1/(s(C1+C2))$, in Figure 5. The additional special-case impedances required to calculate the interaction parameters, $K_N^{(1)}$ and $K_D^{(1)}$, are

$$Z_{N1}|^{(1)}_{Z_2=\infty} = \frac{-e_1(s)}{j_1(s)} \quad (28)$$

$$Z_{D1}|^{(1)}_{Z_2=\infty} = \frac{Z_L + sL_{e1}}{M_1^2(D_1)}. \quad (29)$$

The correction factor of the second open-loop transfer function of interest, $\hat{v}/\hat{d}_2$, can be similarly derived or inferred from the correction factor for the first by symmetry arguments. This leads

[4]N and D historically represent to "numerator" and "denominator" [17]

to:

$$Z_{N1}|_{Z_2=0}^{(2)} = \frac{sL_{e1}}{M_1^2(D_1)} \tag{30}$$

$$Z_{N2}|_{Z_1=0}^{(2)} = \frac{-e_2(s)}{j_2(s)} \tag{31}$$

$$Z_{D1}|_{Z_2=0}^{(2)} = \frac{sL_{e1} + \frac{sL_{e2}Z_L}{Z_L+sL_{e2}}}{M_1^2(D_1)} \tag{32}$$

$$Z_{D2}|_{Z_1=0}^{(2)} = \frac{sL_{e2} + \frac{sL_{e1}Z_L}{Z_L+sL_{e1}}}{M_2^2(D_2)} \tag{33}$$

and the additional special-case impedances required to calculate the interaction parameters, $K_N^{(2)}$ and $K_D^{(2)}$, are

$$Z_{N2}|_{Z_1=\infty}^{(2)} = \frac{-e_2(s)}{j_2(s)} \tag{34}$$

$$Z_{D2}|_{Z_1=\infty}^{(2)} = \frac{Z_L + sL_{e2}}{M_2^2(D_2)}. \tag{35}$$

Note that from the results above, the "numerator interaction parameter" equals one ($K_N^{(i)} = 1$) for each of the two transfer functions. This fact, which is characteristic of the hybrid power system in Figure 5, simplifies the numerical computation of the correction factors, $CF^{(i)}$, because, in that case, the numerator is exactly factorable as follows:

$$CF^{(i)} = \frac{\left(1 + \frac{Z_1}{Z_{N1}|_{Z_2=0}^{(i)}}\right)\left(1 + \frac{Z_2}{Z_{N2}|_{Z_1=0}^{(i)}}\right)}{1 + \frac{Z_1}{Z_{D1}|_{Z_2=0}^{(i)}} + \frac{Z_2}{Z_{D2}|_{Z_1=0}^{(i)}} + K_D^{(i)}\frac{Z_1Z_2}{Z_{D1}|_{Z_2=0}^{(i)}Z_{D2}|_{Z_1=0}^{(i)}}}. \tag{36}$$

In analogy to the impedance inequalities from (18) and (19), the expression for the correction factor in (21) or (36) suggests that the i^{th} open-loop converter transfer function will not be impacted significantly if the following impedance inequalities are met. Recall that meeting these impedance qualities is sufficient but not necessary to ensure stability of the regulated power system.

$$|Z_1| << |Z_{N1}|_{Z_2=0}^{(i)}| \tag{37}$$

$$|Z_2| << |Z_{N2}|_{Z_1=0}^{(i)}| \tag{38}$$

$$|Z_1| << |Z_{D1}|_{Z_2=0}^{(i)}| \tag{39}$$

$$|Z_2| << |Z_{D2}|_{Z_1=0}^{(i)}| \tag{40}$$

*3) **Input Filter Design Approach:*** The input filters in an EIS-capable hybrid power system may be designed to achieve several goals simultaneously:

1) Attenuate converter switching ripple
2) Avoid converter instability
3) Pass or even amplify excitation signals

Goals 1) and 2) are typical of design goals when adding an input filter onto a regulator. Goal 3) is unique to the EIS-capable hybrid system, because the filter must be designed to allow excitation currents to flow from the converter input to the terminals of the fuel cell up to a specified frequency.

For this example, we consider the input filter shown in Figure 13, which includes both the internal input filter components provided on the off-the-shelf Buck converter from Figure 3a as well as the external input filter components that we added, L_{f1} and C_{f1}. The internal input filter components are:

$$C_{f3} = 8.8\ \mu\text{F} \tag{41}$$

$$L_{f3} = 2.2\ \mu\text{H} \tag{42}$$

$$C_{f4} = 26.4\ \mu\text{F}. \tag{43}$$

Having set the pass band and rollover frequencies by choosing

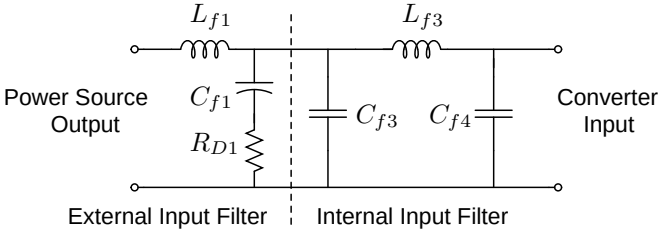

Fig. 13: The input filter for the fuel cell leg.

L_{f1}, the filter transfer function is shown in Figure 14.

The damping leg formed by C_{f1} and R_{D1} in Figure 13 is intended to limit the magnitude peaking in the output impedance of the filter. However, as the impedance of the damping leg decreases it provides a shunt path that diminishes the transmission of excitation currents to the fuel cell terminals. Moreover, due to natural bandlimiting in the system, the designer may actually want to exploit the resonance at the edge of the pass band in Figure 14 to achieve some current amplification at that frequency. Both of these considerations qualitatively lower-bound the damping resistor, R_D, a constraint which directly contends with the impedance inequalities in (37)-(40).

Figure 15 shows a magnitude plot of the special-case impedances for correcting $\hat{v}/\hat{d}_1$ as well as the output impedances from the filters used in our system. Note that the two resonances in Z_o (solid line) correspond to the two resonances

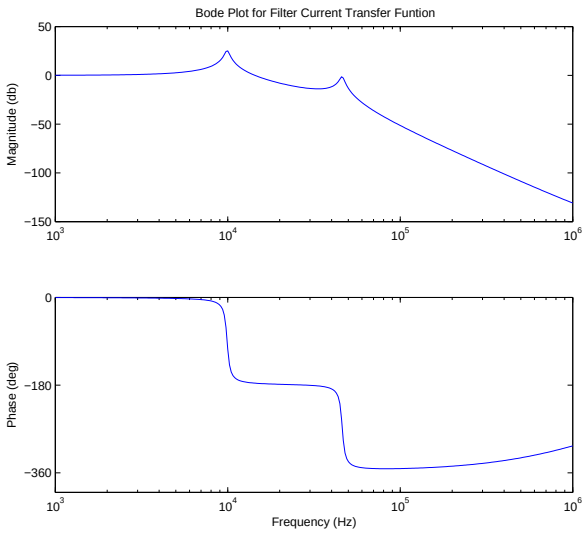

Fig. 14: The current transfer function for the fuel-cell leg input filter

in the filter transfer function of Figure 14. Also note that the plot of special-case impedances suggests that the hybrid system of Figure 5 actually lower-bounds the bandwidth of the input filter to ensure negligible impact on converter dynamics. Because the impedance inequalities in (37)-(40) are not strictly met, as is evidenced by the plot in Figure 15, we need to examine the quantitative impact of the input filters on the converter open-loop transfer functions. In this Section, we assume that the feedback regulated system in Figure 5 is stable without the input filters connected, and that we simply need to verify that adding those input filters does not lead to instability.

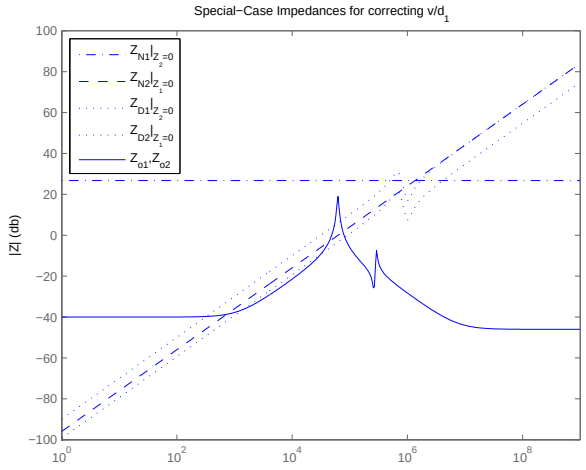

Fig. 15: A frequency plot of the special case impedances for correcting $\hat{v}/\hat{d}_1$ and the input filter output impedances for checking the impedance inequalities in (37)-(40). System parameters: $V_{FC} = 28$V, $V_{batt} = 48$V, V_{out}=12V, $R = 2\Omega$, $L_e = 1\mu$H, $C_e = 1\mu$F

A plot of the correction factors, $CF^{(i)}$, for the i^{th} converter open-loop transfer function from (21) is the most direct way of analyzing the effect of the input filter on system stability. We are generally interested in the additional phase lag in the loop transfer function upon addition of the input filter. More specifically, we are interested in the phase margin, or the phase relative to -180° at the unity gain (0db-crossover) frequency of the entire loop transfer function (including the feedback network) upon addition of the input filters. However, since we assume that we are checking that the input filters do not cause an already stable system to become unstable, we simply need to check the *additional* phase lag which is explicitly shown in the multiplicative correction factor.

For instance, the correction factors, $CF^{(1)}$ and $CF^{(2)}$, for the converter open-loop transfer functions, $\hat{v}/\hat{d}_1$ and $\hat{v}/\hat{d}_2$ respectively, are bode plotted in Figure 16. [5] From the plots, we see that $CF^{(2)}$ introduces a significant additional phase lag near 10^5rps. However, the phase lag will not degrade the phase margin unless that phase lag occurs at the cross-over frequency of the entire regulator loop transfer function. In some cases, i.e. when the impedance inequalities in (37)-(40) are grossly violated, the correction factor will contribute phase lag for a wide band of frequencies likely causing instability. Because the phase lag in this example is contributed for only a narrow range of frequencies we would not expect the voltage-mode feedback loop to become unstable.

[5]The simulated data overlayed in the plots of Figure 16 was extracted from LTSPICE by comparing simulations of the open-loop transfer functions with and without the input filters in place.

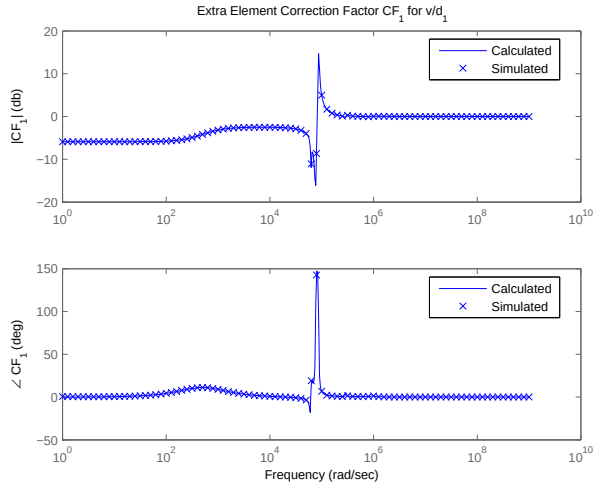

(a) $CF^{(1)}$

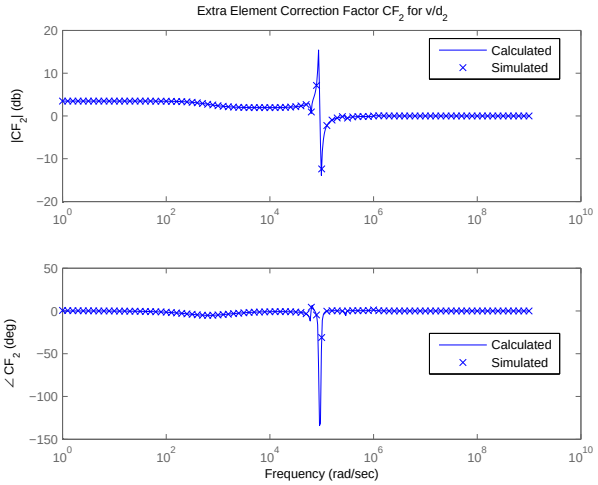

(b) $CF^{(2)}$

Fig. 16: Bode plots of correction factors $CF^{(1)}$ and $CF^{(2)}$ for open-loop transfer functions $\hat{v}/\hat{d}_1$ and $\hat{v}/\hat{d}_2$, respectively. System parameters: $V_{FC} = 28$V, $V_{batt} = 48$V, V_{out}=12V, $R = 2\Omega$, $L_e = 1\mu$H, $C_e = 1\mu$F

The values for the external input filter components were:

$$C_{f1} = 100\ \mu\text{F} \quad (44)$$
$$R_{D1} = 10\ \Omega \quad (45)$$
$$L_{f1} = 6\ \mu\text{H}. \quad (46)$$

These were also the values for the filters used in the system of Figure 3 represented by L_f and C_f. Stability of the real system was verified experimentally.

IV. Experimental Setup

Figure 17 shows an overall schematic of the Siemens 5kW stack, connections to the built-in power electronics and storage,

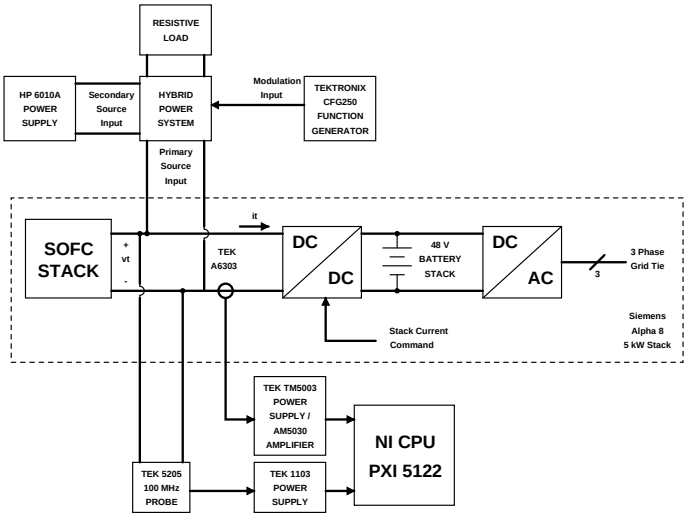

Fig. 17: Schematic illustration of stack, power electronics, and measurements. Components within the dashed line are within the physical envelope of the Siemens Alpha 8 unit.

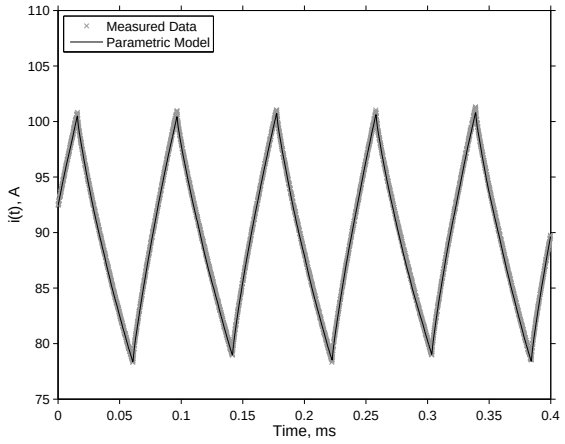

Fig. 18: Measured and predicted stack current as a function of time.

and the locations of our measurements. Under steady-state operation, the unit is remotely configured to regulate current from the stack. This power is then put on the grid through a three-phase inverter. The stack current is measured using a Tektronix A6303 current probe, while the voltage is measured using an isolated, differential Tektronix 5205 probe. Signals from both probes are recorded using a National Instruments data acquisition system with a PXI-5122 14-bit analog to digital converter. Sampling was conducted at a minimum of 2MS/s to avoid under-sampling issues. Figures 19a and 19b show typical data collected from this test setup under steady state operating conditions. The current and voltage levels in Figures 19a and 19b, nominally 100A and 28V, were typical of the stack load during testing.

V. Results

Figure 19 shows typical data collected from the test setup in Figure 17 with a 1kHz exogenous excitation imposed by control of the test power electronics. The triangular ripple current in Fig. 19 at roughly 12 kHz is due to the operation of the front-end boost converter in the Siemens power management system. The current and voltage levels in Fig. 19, nominally 90A and 28V, were typical of the stack load during testing.

Figure 20 shows Nyquist plots of the impedance $\hat{Z}(j\omega)$ obtained from the response of the stack to the built-in power electronics ripple and the power electronic test signal. The plots were prepared according to the convention for electrochemical impedance spectroscopy results. Fig. 20a shows a overall plot representing impedances for all frequencies with significant content. The discete clusters correspond to harmonics of the triangular boost-converter switching waveform, while the more continuous low-frequency data shows the response to the test signal. As the frequency of the harmonics increases, the amplitude decreases, and the variance in the impedance estimate increases. Fig. 20b is an expanded view of the low frequency portion corresponding to the exogenous excitation. The arc shape of the curve in Fig. 20b is consistent with the series connection of parallel RC elements often used in equivalent circuit models of fuel cells.

Data corresponding to a 1kHz power electronic excitation were used to identify the parametric model in II-C. The parameter estimates were $V_{oc} = 34.1V$, $R = 0.0690\Omega$, and $L = 0.43\mu H$. These results compare favorably to those in [5], where the values for these parameters based on data taken months earlier were found to be $V_{oc} = 34.7V$, $R = 0.0677\Omega$, and $L = 0.471\mu H$. The decrease in voltage and increase in resistance are likely due to the gradual degradation of stack performance observed over this time period. The latest parameters were used for an output-error prediction of the time-domain current waveform in response a 5.4 kHz excitation. This cross-validation result is shown in Fig. 18.

Acknowledgments

The authors gratefully acknowledge the support of NSF award #0547616 and MSU-HiTEC. MSU-HiTEC is funded by the United States Department of Energy (USDOE) under Award No. DE-AC06-76RL01830. However, any opinions, findings, conclusions, or recommendations expressed herein are those of the author(s) and do not necessarily reflect the views of the DOE.

The authors would like to thank The Grainger Foundation, the U.S. Department of Energy (DOE) and ARPA-E for their generous support.

References

[1] S. K. Mazumder, K. Acharya, C. L. Haynes, R. Williams, M. R. v. S. Jr., D. J. Nelson, D. F. Rancruel, J. Hartvigsen, and R. S. Gemmen, "Solide-oxide-fuel-cell performance and durability: Resolution of the effects of power-conditioning systems and application loads," *IEEE Transactions on Power Electronics*, vol. 19, no. 5, pp. 1263–1278, September 2004.

[2] B. W. Q. Huang, R. Hui and J. Zhang, "A review of ac impedance modeling and validation in sofc diagnosis," *Electrochimica Acta*, vol. 52, no. 28, pp. 8144–8164, November 2007.

[3] P. P. T. S. E. Ramschak, V. Peinecke and V. Hacker, "Detection of fuel cell critical status by stack voltage analysis," *Journal of Power Sources*, vol. 2006, pp. 837–840, October 2006.

[4] R. S. Gemmen, "Analysis for the effect of inverter ripple current on fuel cell operating condition," *Transactions of the ASME*, vol. 125, pp. 576–585, May 2003.

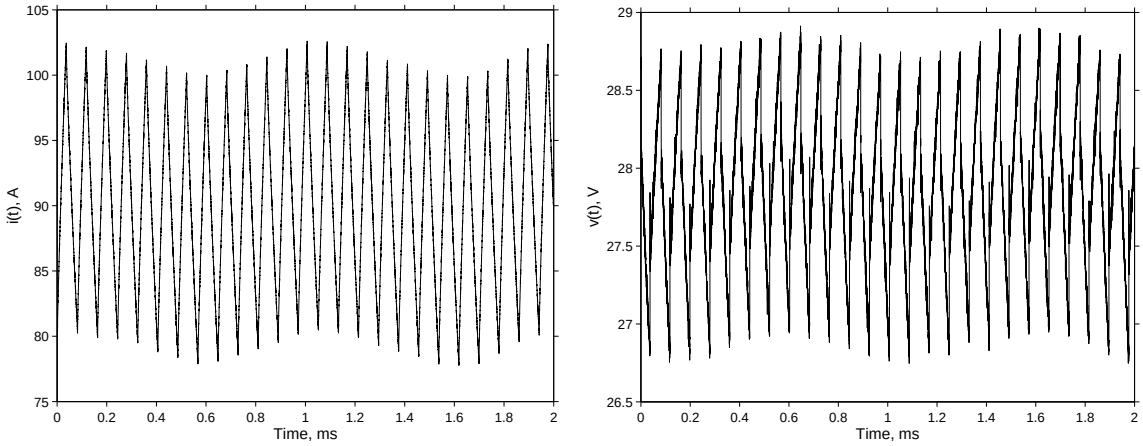

(a) Stack current as a function of time.

(b) Stack voltage as a function of time.

Fig. 19: Stack current and voltage, measured as indicated in Fig. 17. The triangle current waveform in 19a is due to the operation of the DC/DC converter in the system. The corresponding voltage of the stack appears in 19b.

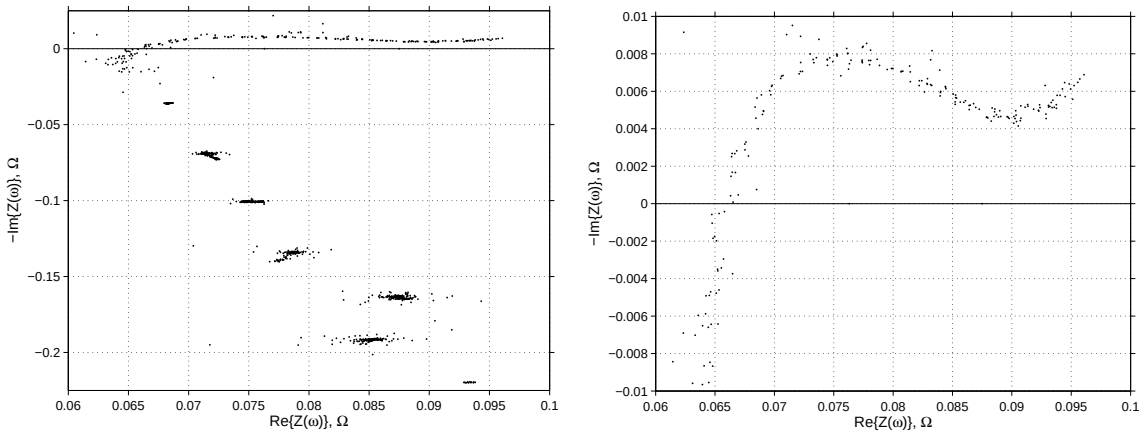

(a)

(b)

Fig. 20: Whole stack impedance spectroscopy results. (a) Stack response to ripple current and power electronic test signal. (b) Low-frequency portion of stack response showing response to power electronic test signal.

[5] E. Seger and S. R. Shaw, "In-situ electrical terminal characterization of a 5 kw solid oxide fuel cell stack," *Submitted for publication in the IEEE Transactions on Energy Conversion*, 2010.

[6] C. Gabrielli, "Use and application of electrochemical impedance techniques," vol. Technical Report 43.

[7] N. Wagner, W. Schnurnberger, B. Müller, and M. Lang, "Electrochemical impedance spectra of solid-oxide fuel cells and polymer membrane fuel cells," *Electrochimica Acta*, vol. 43, no. 24, pp. 3785–3793, 1998.

[8] L. G. A. T. Romero-Castañón and U. Cano-Castillo, "Impedance spectroscopy as a tool in the evaluation of mea's," *Journal of Power Sources*, vol. 118, pp. 179–182, May 2003.

[9] E. Barsoukov and J. R. MacDonald, *Impedance Spectroscopy Theory, Experiment, and Applications*. John Wiley and Sons, Inc., 2005.

[10] R. Johansson, *System Modeling and Identification*. Prentice-Hall, Inc., 1993.

[11] D. J. Hall and R. G. Colclaser, "Transient modeling and simulation of a tubular solid oxide fuel cell," *IEEE Transactions on Energy Conversion*, vol. 14, no. 3, pp. 749–753, September 1999.

[12] M. H. N. C. Wang and S. R. Shaw, "Dynamic models and model validation for pem fuel cells using electrical circuits," *IEEE Transactions on Energy Conversion*, vol. 20, no. 2, pp. 442–451, June 2005.

[13] S. Pasricha and S. R. Shaw, "A dynamic pem fuel cell model," *IEEE Transactions on Energy Conversion*, vol. 21, no. 2, pp. 484–490, June 2006.

[14] R. Middlebrook and S. Cuk, "A general unified approach to modeling switching-converter power stages," *International Journal of Electronics*, vol. 42, pp. 521–550, June 1977.

[15] R. Middlebrook, "A general unified approach to modelling switching dctodc converters in discontinuous conduction mode," *IEEE Power Electronics Specialists Conference*, vol. 32, no. 3, pp. 36–57, 1977.

[16] ——, "Input filter considerations in design and application of switching regulators," *IEEE Industry Applications Society Annual Meeting*, no. 76CH1122-1-IA, p. 366382, 1976.

[17] R. W. Erickson and D. Maksimovic, *Fundamentals of Power Electronics, Second Edition*. Springer Science+Business Media, LLC., 2001.

[18] R. Middlebrook, "Modelling and analysis methods for dc-to-dc switching converters," *IEEE International Semiconductor Power Converter Conference*, pp. 90–111, 1977.

[19] J. J. Cooley, Ph.D. dissertation, Massachusetts Institute of Technology, To be published 2010.

[20] R. Middlebrook, "Design techniques for preventing input-filter oscillations in switched-mode regulators," *Proc. Fifth National Solid-State Power Conversion Conference (Powercon 5)*, p. A3.1A3.16, May 1978.

[21] ——, "Null double injection and the extra element theorem," *IEEE Trans. on Education*, vol. 32, no. 3, pp. 90–111, August 1989.

[22] ——, "The two extra element theorem," *Proc. IEEE Frontiers in Education*, pp. 702–708, Sept. 1992.